Modeling Velocity Recordings of the M_w 6.0 South Napa, California, Earthquake: Unilateral Event with Weak High-Frequency Directivity

by František Gallovič

ABSTRACT

On 24 August 2014, an M_w 6.0 earthquake struck the Napa area in the north San Francisco Bay region, causing one fatality and damaging many older buildings in the Napa area. First, I employ low-frequency data (0.05–0.5 Hz) from 10 near-fault strong-motion stations to perform slip inversion, revealing (in agreement with other studies) rupture propagating up-dip and unilaterally along the fault with a dominant shallow asperity. Then I generate broadband synthetics (0.05–5 Hz) using an advanced Ruiz integral kinematic (RIK) source model (Ruiz *et al.*, 2011) and a 1D velocity model. The RIK model is composed of randomly distributed overlapping subsources with a fractal number–size distribution. The particular distribution of the RIK subsources is constrained by the low-resolution slip model from the inversion. Besides providing stable omega-squared spectral decay at high frequencies, the RIK model is able to reproduce the frequency-dependent directivity effect with adjustable strength. Comparison of the synthetic velocity waveforms with the observed data shows that the smallest modeling bias and variance is achieved by a rupture model with complex rupture propagation and thus weak high-frequency directivity. I link my findings with other studies, including analog experiments by Day *et al.* (2008), suggesting that this feature is rather common to earthquake sources.

Online Material: Tables of station locations and crustal model, and figures of synthetic seismograms and their smoothed Fourier spectra for all directivity models.

INTRODUCTION

The South Napa earthquake occurred on 24 August 2014 at 10:20:44 UTC in California, 6 km northwest of American Canyon and 9 km southwest of Napa. The event triggered ShakeAlert and G-larmS early warning systems, sending an alert to San Francisco about 10 s prior to the start of the strongest shaking (Grapenthin *et al.*, 2014). Quick estimates of the ground motions (ShakeMap) and the impact on the population (PAGER) were released 11 and 13 min after the earthquake, respectively. The earthquake caused one fatality and damaged many older buildings in the Napa area (Brocher *et al.*, 2015).

Routine seismological and geodetical analyses were performed by world agencies, including several United States institutions. Basic parameters of the event are summarized (e.g., at the U.S. Geological Survey [USGS] website; http://earthquake.usgs.gov, last accessed October 2015), including the location and the centroid moment tensor (CMT). The event ruptured the West Napa fault belonging to the San Andreas fault system. The fault is known to be active; the USGS National Seismic Hazard Maps depicts the epicentral region to likely experience strong shaking in the future. Quick slip inversions were provided at the USGS webpage by D. Dreger (University of California, Berkeley) using regional seismic data and by W. Barnhart (USGS National Earthquake Information Center) using the Global Positioning System and Interferometric Synthetic Aperture Radar data. Those preliminary results have been refined and published in an *SRL* focus section (Barnhart *et al.*, 2015; Dreger *et al.*, 2015). Together with other models published so far (Ji *et al.*, 2015; Melgar *et al.*, 2015; Wei *et al.*, 2015) show, generally speaking, that the event was unilateral northward toward the city of Napa, having significant asperity at shallow depths (< 5 km) with longer rise times at the place where 40–46 cm surface fault slip was observed (Brocher *et al.*, 2015).

Such a unilateral event is expected to exhibit a strong source directivity effect, amplifying the ground motions in the direction of the rupture propagation (northward) and broadening of velocity pulses, especially at the fault-normal (F-N) components (e.g., Somerville *et al.*, 1997). Therefore, the directivity effect is of great interest for earthquake engineers. Baltay and Boatwright (2015) have analyzed residuals of the South Napa earthquake observed data with respect to ground-motion prediction equations (GMPEs). They have shown that while the residuals of pseudospectral acceleration (PSA) at 3 s exhibit clear amplification due to the directivity
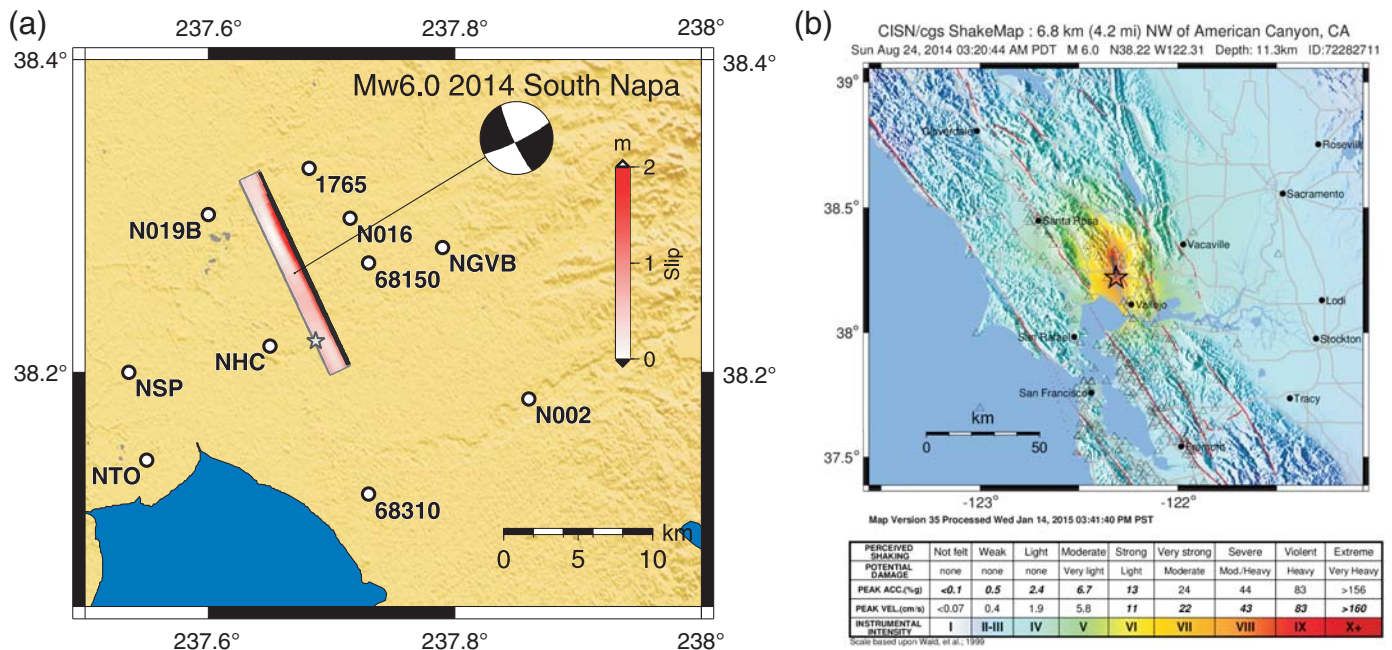
▲ **Figure 1.** (a) Map of the Napa earthquake epicentral area showing stations (circles), the event hypocenter (star), focal mechanism (beachball), and the fault model (rectangle) with the top (black line) reaching 400 m below the surface. Stations 1765, N016, and 68150 are located in the city of Napa. The slip model from inversion (see also Fig. 2) is shown on the fault in the shaded scale. (b) Instrumental intensity ShakeMap (see Data and Resources) with apparently no directivity effect, except for the elongation related to the finite extent of the fault (gray line).

effect, those at 0.3 s and the peak ground accelerations (PGAs) do not. This suggests that the source directivity effect is reduced at higher frequencies. At midfrequencies, the residuals of PSA at 1 s and peak ground velocities (PGVs) show indeed a less-pronounced directivity effect, being also perhaps overlaid by a fault-zone-guided wave effect (Baltay and Boatwright, 2015). Instrumental intensity ShakeMaps, obtained by interpolating recorded ground motion, do not exhibit clear manifestation of the northward source directivity effect, being characterized only by elongation due to the finite extent of the fault (Fig. 1). Stations NHC and N019B, located at similar distance from the largest slip patch (Fig. 1) but at opposite directions with respect to the rupture propagation, experienced almost the same PGV (0.58 and 0.63 m/s, respectively) and PGA (0.40g and 0.34g, respectively). Moreover, although the F-N component at the directive stations N019B and 1765 exhibit broader velocity pulses due to the strong low-frequency directivity effect, their amplitudes (related to the perhaps weaker high-frequency directivity) are comparable or only slightly larger than those at the respective fault-parallel (F-P) components. I emphasize that this is in contradiction to the classical source directivity models that predict amplification of the motion up to 5–10 times at all frequencies larger than the corner frequency, which is definitely not observed for this particular event. Although wave-propagation effects could have contributed to some extent to the amplification of the ground shaking south from the event (e.g., NHC is situated in deeper sediments than N019B), it is very

likely that the source effect also had to contribute in the almost full removal of the directivity effect at high frequencies. Proper modeling of such frequency-dependent directivity effect is the key point of this article.

Because many high-quality recordings were written by stations at near-fault distances for this earthquake, it is a unique opportunity to test source models with various directivity strengths. The article consists of two parts. In the first one, I perform slip inversion by the recently introduced technique by Gallovič et al. (2015) using local strong-motion data at relatively low frequencies (0.05–0.5 Hz). In the second part, I generate broadband synthetics (0.05–5 Hz) using an advanced kinematic source model introduced by Ruiz et al. (2011), hereinafter denoted as the Ruiz integral kinematic (RIK) model. High-frequency ground-motion modeling requires a stochastic component. In RIK, it is represented by a random distribution of overlapping subsources with fractal number-size distribution that compose the source model. The particular distribution of the RIK subsources is constrained by the retrieved low-frequency slip model from the inversion. Besides the fact that the RIK model provides consistently omega-squared spectral decay at high frequencies, it allows for modeling the frequency-dependent directivity effect with various strengths. The model with the weakest (high-frequency) directivity, being characterized by complex rupture propagation along the fault, is demonstrated to provide synthetics with the smallest modeling bias and variance when compared with the velocity recordings.

Table 1
Parameters of the Earthquake Source Model Including Details of the Model Setup for the Low-Frequency Slip Inversion and the Ruiz Integral Kinematic (RIK) Model Used in the Broadband Modeling

	Parameter	Definition
General Source Parameters	Origin time	24 August 2014, 10:20:44
	Epicenter location	38.220° N, 122.313° W
	Hypocentral depth	10 km
	Fault size	15 km × 10 km
	Fault mechanism	Strike 155°, dip 82°, rake −172°
	Scalar seismic moment	1.6×10^{18} N·m
	Location of hypocenter on the fault	12.5 km along strike, 0 km from the fault bottom
Parameters Specific to the Slip Inversion	Fault discretization	750 m × 625 m
	Smoothing parameter (σ_D)	0.1 m (see Gallovič et al., 2015)
Parameters Specific to the RIK Model	Fault discretization	100 m × 100 m
	Slip pulse width (L_0)	3 km (weak- and moderate-directivity model); 0.75 km (Strong-directivity model)
	Number of subsources	925
	Subsource radii	2.5–0.2 km
	Earthquake stress drop	1 MPa
	Parameter a (see equation 2)	0.5
	Rupture velocity	$0.8 \times V_S$ (V_S follows the velocity depth profile; Ⓔ see Table S2)

DATA AND CRUSTAL MODEL

I have downloaded the raw accelerometric data from the database of the Center for Engineering Strong Motion Data (CESMD, see Data and Resources) recorded at stations distant up to 15 km from the fault. Figure 1a shows the station distribution together with the earthquake hypocenter and fault. The stations are also listed in Ⓔ Table S1 (available in the electronic supplement to this article), together with the network and site information as available in the CESMD database. Unfortunately, only two stations have been assigned National Earthquake Hazards Reduction Program (Dobry et al., 2000) site classes, namely stations 68150 (class D) and 68310 (class C). Regarding the latter station, it is the deepest station from a geotechnical array (at 44.5 m) in Vallejo. I note that there are other two nearby stations available in Vallejo (California Geological Survey station 68294, Broadway and Sereno, and USGS station 1759, Fire Station). However, because for my purpose the recordings are very similar with each other, I prefer to use only the borehole station as being least affected by the site effects.

The acceleration data were detrended, band-pass filtered using one-way (causal) Butterworth filter of the fourth order, once- or double-integrated to velocity or displacements, respectively, and eventually undersampled. The high-pass filtering at 0.05 Hz removes the low-frequency part of the wavefield that is corrupted by the instrumental noise. The low-pass filter depends on the particular application. In the slip inversion, I assume the filtering frequency at 0.5 Hz because the 1D crustal model considered (see below) is not able to model Green's functions (GFs) at higher frequencies with the required accuracy. For the broadband modeling, I consider filtering frequency at 5 Hz as sufficient for the velocity recordings and to limit the computational expense. The horizontal components were rotated to the F-P and F-N components. No time shifts were applied.

For the wave-propagation modeling, I use a modification of the 1D layered velocity model GIL7 (Stidham et al., 1999; see Ⓔ Table S2). The original model has 1-km-deep subsurface layer with S-wave velocity of 1.5 km/s. Because the station sites have lower subsurface velocities, I have introduced two additional layers with subsurface velocity representing soft-rock site properties (see Ⓔ Table S2). Nevertheless, I note that, in the 1D modeling, such modifications lead to just minor amplification at higher frequencies and thus are not critical in the modeling. Full wavefield GFs are calculated using the discrete wavenumber technique (Axitra code, Kennett and Kerry, 1979; Bouchon, 1981; Coutant, 1989). No stochastic GFs are used throughout the whole study.

SLIP INVERSION

Basic source parameters are listed in Table 1. I adopt the USGS location parameters (see Data and Resources) and the mechanism from the Northern California Earthquake Data Center (see Data and Resources). The planar fault is 15 km × 10 km,
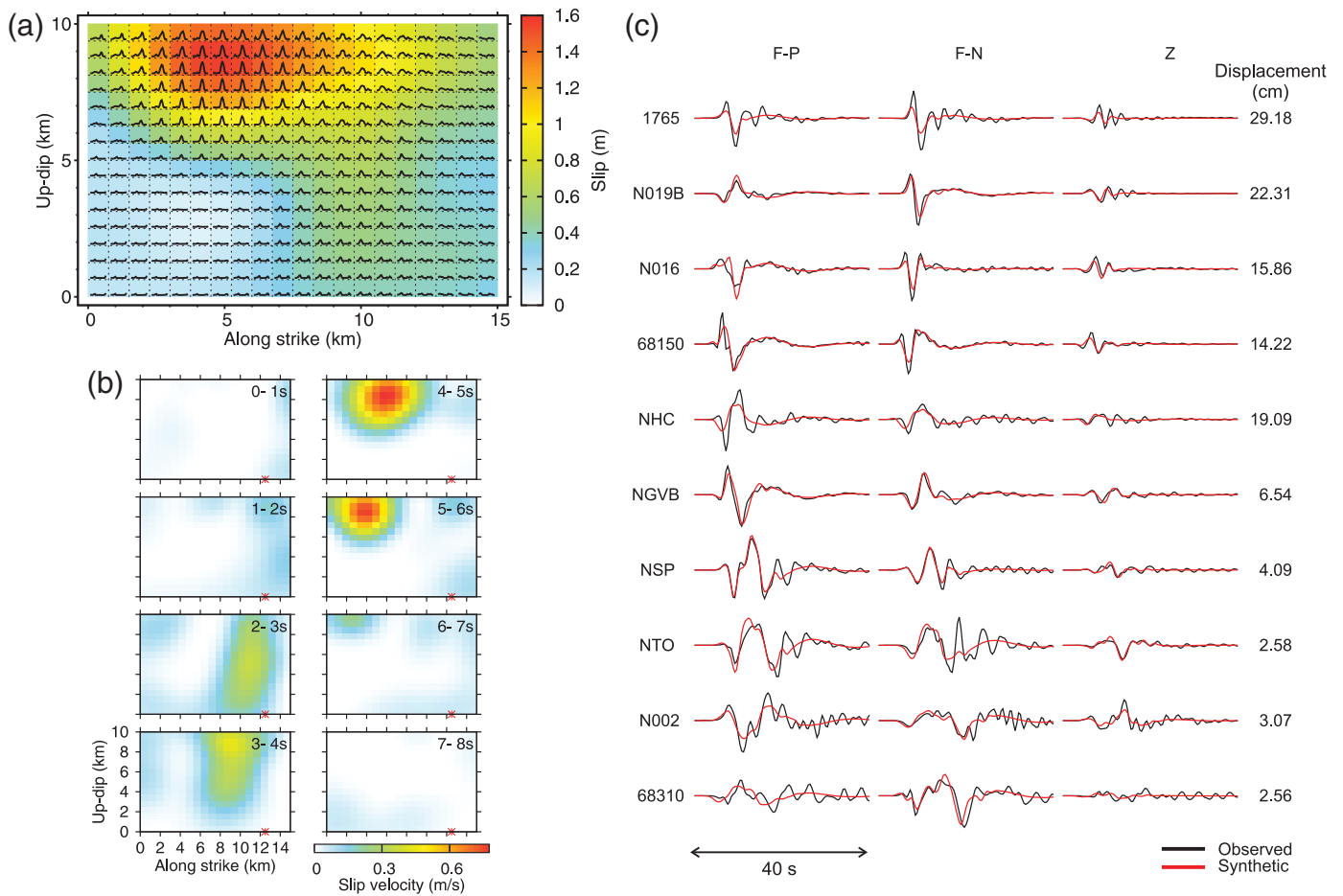
▲ **Figure 2.** Result of the linear slip inversion by the Gallovič *et al.* (2015) method considering slip-rate positivity and spatial smoothing by means of a prior covariance matrix. (a) Final slip is shown using the shaded scale, with superimposed slip rates as inferred from the inversion; the duration of the slip rates cover 0–8 s after the hypocentral time. (b) Snapshots of the rupture propagation suggesting up-dip and against-strike propagation (northward). Asterisks denote the hypocenters (not considered in the inversion). (c) Comparison of observed and synthetic displacement waveforms (0.05–0.5 Hz) corresponding to the inverted source model (variance reduction 61%). (F-P, fault-parallel component; F-N, fault-normal; and Z, vertical component.) Station names are to the left (see Fig. 1 for their location).

with the hypocenter located at its bottom edge at a depth of 10 km.

I use the recently introduced slip inversion technique by Gallovič *et al.* (2015) exploiting the linear formulation of the forward problem. The method has been recently tested on a source inversion validation benchmark test (Gallovič and Ampuero, 2015) and applied to the 2014 Cephalonia earthquake doublet (Sokos *et al.*, 2015). Parameters of the inverse problem are the slip-rate functions discretized in time and along the fault. The slip rates span an 8-s-long time window, starting at the hypocentral time; the nucleation point is not prescribed in the inversion. The inverse solution is regularized by (1) spatial smoothing by means of a prescribed prior covariance function with the k^{-2} spectral decay (k being the wavenumber) and (2) positivity constraint by means of using the nonnegative least-squares approach by Lawson and Hanson (1974) to minimize the L2 misfit function in displacements filtered between 0.05 and 0.5 Hz. The weight of the smoothing constraint is set

to $\sigma_D = 0.1$ m (for the formal definition of σ_D, see Gallovič *et al.*, 2015), which corresponds to rather stronger smoothing. Gallovič *et al.* (2015) demonstrated by means of synthetic tests in a very similar setting (source–station geometry, frequency range, etc.) that the use of low-frequency waveforms together with the stronger smoothing prevents the occurrence of artificial slip-rate peaks when the 3D structural model is approximated by a 1D velocity model. This suggests that the inversion does not require any temporal alignment of the GFs, thus providing a robust inversion result. This is important because, especially at near-source stations, such alignments should, in principle, vary along the fault as the propagating wavefields sample different volumes of the velocity structure.

The result of the inversion is shown in Figure 2. In particular, Figure 2a shows the final slip distribution overlaid by the individual slip-rate functions from the inversion. The slip distribution is characterized by a large slip patch at rather shallow depths. Figure 2b displays the evolution of the inverted

rupture model in terms of slip-rate snapshots. I note that the inversion result cannot be taken at face value as discussed by Gallovič *et al.* (2015) due to the generous model parameterization, applied smoothing, and limited frequency range. Regarding the former, because the rupture can generally occur at any place at any time, the inferred model contains some "ghost" features, presumably due to imperfections in GFs. Despite this issue, the general feature of the result is that the rupture propagated from the hypocenter upward and against the fault strike (northward). Unfortunately, further details are hard to reveal. Indeed, the inferred source model represents the true model after spatial smoothing applied at each time instance (see the synthetic tests by Gallovič *et al.*, 2015), requiring careful interpretation of the inferred rupture image. The large asperity is rather biased toward too-shallow depths (note that the surface fault traces showed 40–46 cm large displacements). Inspecting the snapshots in Figure 2b, the slip rates seem negligible during the first 2 s, suggesting rather low slip or slip rates at the hypocenter. Larger slip rates then occur ~5 km from the hypocenter. After another 3 s, the shallow asperity located ~12 km from the hypocenter is slipping at larger slip velocities. These observations can help to roughly estimate that the rupture speed is approximately ~2.5 km/s, noting that this value is rather underestimated due to the severe spatial smoothing as shown by Gallovič *et al.* (2015) using synthetic tests. Figure 2c shows the comparison between the observed and synthetic displacements. The fit is best at the near-fault stations. At the distant stations the 1D model does not explain the short-period oscillations and later arrivals, being presumably related to the complexity in the wave propagation in the heterogeneous crust.

The inferred slip model is close to the model by Wei *et al.* (2015) and geodetic model by Melgar *et al.* (2015). Seismic and seismogeodetic model by Melgar *et al.* (2015), as well as models by Barnhart *et al.* (2015) and Dreger *et al.* (2015), are characterized by a deeper main asperity (3–8 km). Ji *et al.* (2015) inferred a model with an ellipsoidal slip of approximately 12 km × 5 km oriented toward top left from the hypocenter. The slip rates inferred by Melgar *et al.* (2015) are of similar shape as those retrieved in this study but with rise time approximately two times shorter (1 s). All the models consistently show up-dip and northward rupture propagation. I note that while the source model derived here is smoother than the others, it is not sensitive to minor changes of the crustal model (i.e., no artificial time shifts of the GFs are required).

RUIZ INTEGRAL KINEMATIC (RIK) SOURCE MODEL

Model Description
Here, I use an advanced kinematic source model introduced by Ruiz *et al.* (2011), the RIK model. It was developed for earthquake ground-motion simulations utilizing the representation integral in the full frequency band (no composite or stochastic modeling needed) and providing omega-squared spectral decay at high frequencies. I applied some simplifications and minor

modifications to the original method, following specific properties of my particular application (see below). The RIK model is composed of randomly distributed circular subsources with fractal number-size distribution with dimension $D = 2$, which is the same as considered in other kinematic models (e.g., Zeng *et al.*, 1994; Gallovič and Brokešová, 2007). In the present model, kinematic properties (including the rupture propagation) are prescribed individually to each of the subsources, and thus each subsource is characterized by its own slip-rate functions along its areal extent. The total slip rates of the RIK model are eventually evaluated on a dense regular discretization grid along the fault by summing up slip-rate contributions from all the subsources.

Regarding the subsource distribution, I introduce a minor simplification to the original Ruiz *et al.* (2011) approach, considering that subsource radii R are equal to integer fractions n of the fault width W, that is, $R = W/n$. For the particular number-size distribution, the number of subsources at level n is equal to $2n - 1$. The subsources are distributed randomly along the fault, following a prescribed spatial probability density function (PDF), which is considered equal to the normalized slip distribution from the inversion (see above). The subsources have the crack-model slip distributions Δu^R, that is,

$$\Delta u^R(\rho) \sim \sqrt{R^2 - \rho^2} \quad \text{if } \rho < R \quad \text{and}$$
$$\Delta u^R(\rho) = 0 \text{ otherwise,} \tag{1}$$

in which ρ is the distance from the subsource center. The constant of proportionality in equation (1) is determined so that the total seismic moment fits the prescribed scalar seismic moment M_0. This fractal decomposition of the source model implies that the slip decays with k^{-2} at high wavenumbers k (Gallovič and Brokešová, 2007; Ruiz *et al.*, 2011), implying k^{-1} decay of the stress distribution, which was shown by means of theoretical considerations as physically plausible (Andrews, 1980).

The rupture is assumed to propagate in the form of a slip pulse of width L_0 with the Brune's pulse (Brune, 1970) as the slip-rate function. I note that if rise time was constant, the source spectrum would decay as omega squared only up to the reciprocal of the rise time, after which the spectrum would decay faster due to the low-pass filtering effect of the consider slip-rate function. To correct for this, Bernard *et al.* (1996) introduced the concept of the wavenumber-dependent rise time. In particular, in the RIK model, the rise time depends on subsource radius R as

$$\tau(R) = \tau_{\max} = aL_0/v_r \quad \text{if } 2R > L_0 \quad \text{and}$$
$$\tau(R) = a(2R)/v_r \text{ otherwise,} \tag{2}$$

in which $a \sim 1$ is a free parameter and v_r is the rupture velocity equal to a prescribed fraction of the local S-wave velocity following the crustal model considered. Consequently, one avoids unrealistically strong ground motions when dealing with subsurface rupture because the rise time generally increases with

the decreasing depth (Graves and Pitarka, 2010). Furthermore, the dependence of the rise time on the subsource radii (also called the *k*-dependent rise time) also has implications for the strength of the directivity effect. As discussed by Bernard *et al.* (1996) and Gallovič and Brokešová (2004), the source spectral amplitudes between roughly the corner frequency and the reciprocal of the maximum rise time ($1/\tau_{\max}$) are proportional to C_d^2, in which $C_d = 1/(1 - \alpha \cos \theta)$ is the classical directivity coefficient, with α representing the ratio of rupture and shear wavespeeds and θ being the station angle from the rupture direction. At frequencies larger than $\sim 1/\tau_{\max}$, the directivity effect is reduced to C_d^1, while preserving the omega-squared spectral decay. I also note that the use of the *k*-dependent rise time implies a positive correlation between the slip and the rise time as found in dynamic source simulations (Schmedes *et al.*, 2010).

In terms of the rupture propagation, Ruiz *et al.* (2011) introduced a concept of small- and large-scale rupture fronts. In particular, each point on subsources with radius $R > L_0$ starts to slip upon arrival of the macroscopic rupture front from the hypocenter. Contrarily, each smaller subsource has its own random point, from which a small-scale rupture is initiated after the random point is reached by the macroscopic rupture front. In other words, rupture time at a given point on the small subsource is a sum of the arrival time of the macroscopic rupture front to the random point and the time delay corresponding to the small-scale rupture propagation from the random point. This way, the directivity effect is weakened even further, to effectively $C_d^0 = 1$ (i.e., is isotropic).

All source parameters describing the RIK model are listed in Table 1. The values of the rupture velocity, slip pulse width, and rise-time parameter *a* of equation (2) were found by trial-and-error modeling to best fit the observed duration of the major velocity pulses, their peak values, and the spectral content at all the stations. In particular, the rupture velocity is equal to $0.8V_S$, which is consistent with other studies (Dreger *et al.*, 2015; Wei *et al.*, 2015). Because of the large uncertainty of the strongly smoothed source model obtained by the low-frequency inversion, I employ only the final slip distribution (Fig. 2a) as the PDF function for the random distribution of the subsources along the fault plane. Figure 3a shows the distribution of just the largest subsources (for clarity), together with the resulting slip distribution. I note that the RIK model has much smaller slip values at the surface than the slip model from the low-frequency inversion (compare Fig. 3a and 2a). Conclusions regarding the directivity effect (as drawn below) are based exclusively upon the RIK model and are thus not compromised by the rather biased surface slip values from the slip inversion.

In the following, I test three models with various strengths of the directivity effect. The first one, the weak-directivity model, is the one described above. The moderate-directivity model differs in that the small-scale rupture front on the subsources is the same as the large-scale front, which makes the model close to the classical kinematic models with a single rupture front. The third model, with the strong directivity, has a narrower slip pulse width, that is, shorter maximum rise time (see Table 1).

Moment rate functions corresponding to the three directivity models are displayed in Figure 3b in both the temporal and spectral domains. The Fourier spectrum of the source time functions is well fitted by the Brune model (Brune, 1970) with stress drop of 1 MPa (Fig. 3b), which is close to the typical regional value of 5 MPa as determined by Baltay and Hanks (2014). Figure 3c shows examples of slip rates at two time instances to visualize the difference between the rupture propagation of the three models. Basically, in the weak-directivity model, the instantaneous slip-rate maxima are less coherently aligned along the rupture front than in the other two models. The strong-directivity model has a narrower pulse width with larger slip-rate maxima. Figure 3d displays also the apparent moment rate functions at two stations, one in the forward (N019B) and one in the backward (68310) directivity area. Although the apparent time functions of the three models are similar at long periods, they differ in the strength of the short-period oscillations (especially in the forward-directivity station N019B) owing to the different style of the rupture propagation. This is clearly visible in the apparent acceleration source spectra in Figure 3d. Because of the short maximum rise time, the strong-directivity model has the C_d^2 spectral amplification in a broad range of frequencies. Although the difference between the weak- and moderate-directivity models is not large, the former has slightly smaller and larger amplitudes at the forward- and backward-directivity stations, respectively, due to the additional random propagation inside the individual subsources. A similar effect is achieved when considering radiation from the centers of the subsources, as considered in the composite source models (e.g., Zeng *et al.*, 1994; Gallovič and Brokešová, 2007).
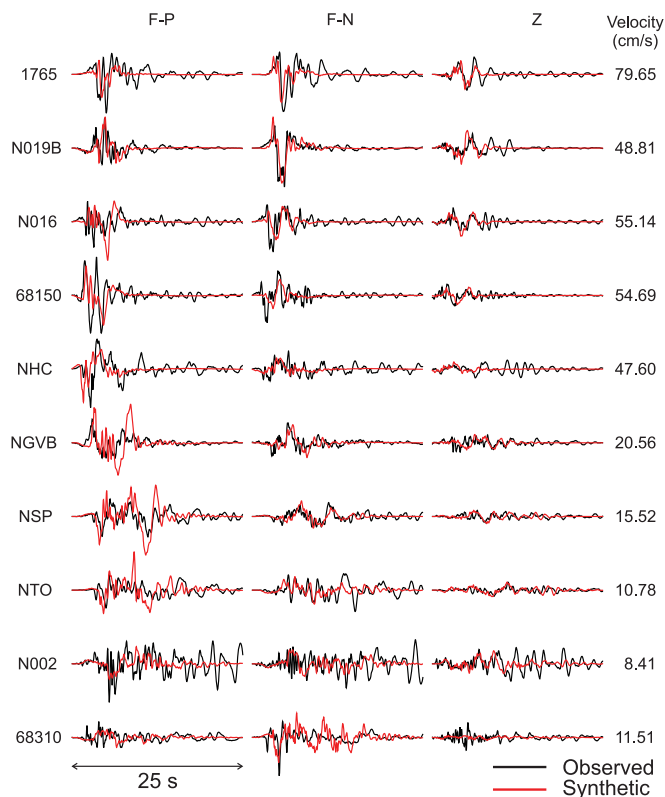
Modeling Results (Weak-Directivity Model)

Figure 4 shows comparisons between the observed and synthetic velocity waveforms in the frequency range 0.05–5 Hz for the weak-directivity model. Because of the fact that at such large frequencies both the source and propagation medium have a fractal (random) nature, a model cannot capture all details of the velocity records. Thus the point is not to fit the observed waveforms in detail (i.e., wiggle for wiggle), but rather to match their basic characteristics in the temporal domain and their spectral response. Below, I discuss that this is the case of the model presented here.

In particular, at the *Z* component, the peak values and the dominant period of the first arrivals are correctly captured by the model, except for station 68310, the amplitude of which is underestimated significantly. At the F-N component, the forward-directivity velocity pulse is fit very well at station N019B. Interestingly, the model captures (although not perfectly) the more complex shape of the pulse at station 1765, lying just on the opposite side of the fault (Fig. 1) and thus being a consequence of the up-dip directivity. Stations N016 and 68150, lying close to the central part of the fault, exhibit two-sided pulses at the F-N component, which are explained relatively
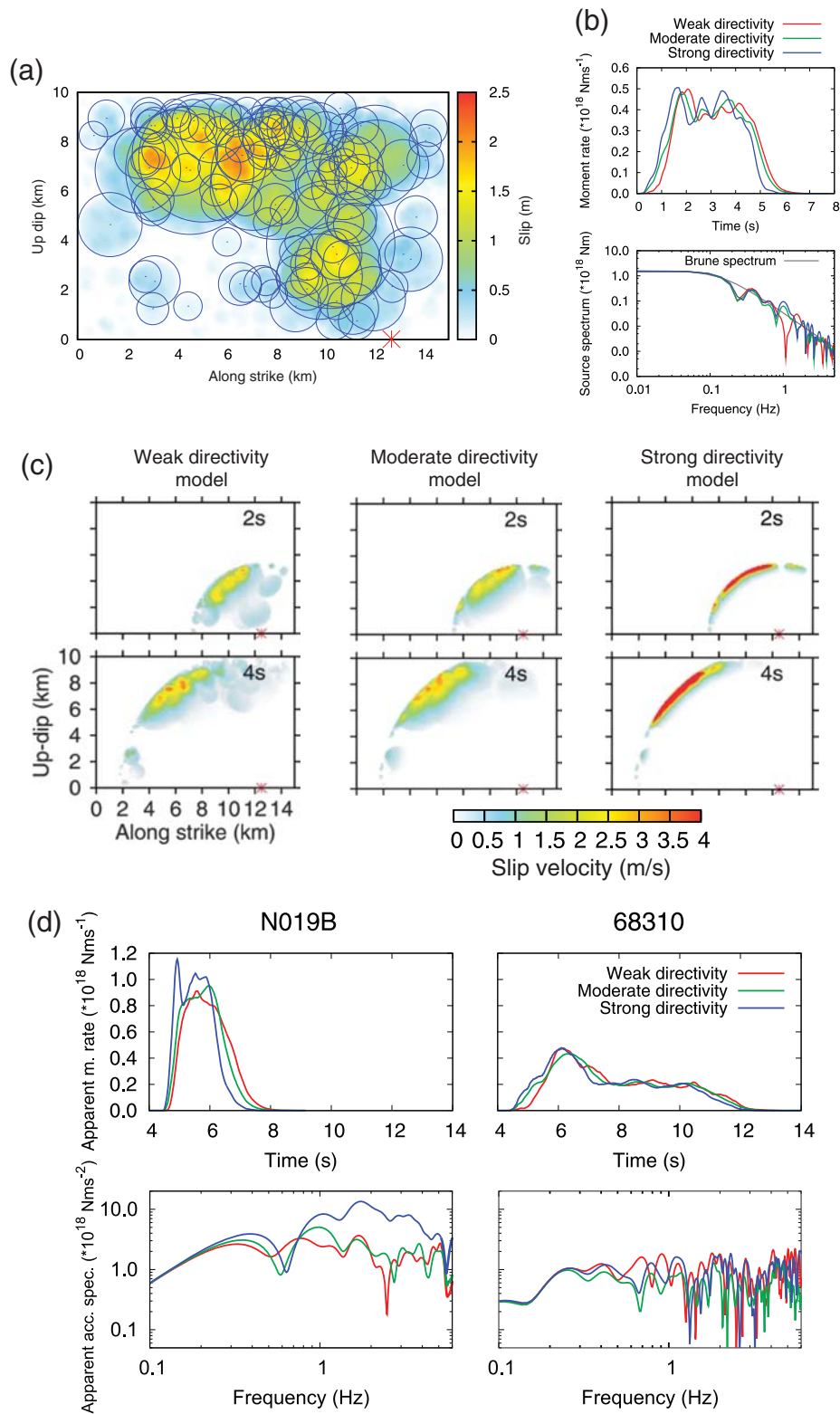
▲ **Figure 3.** Properties of the Ruiz integral kinematic (RIK) model used in the velocity waveform modeling (0.05–5 Hz). (a) Slip model (shaded scale) built by randomly distributing subsources (circles) with fractal number-size distribution (see the Model Description section for details); only the largest subsources are plotted for the sake of clarity. The red asterisk denotes the hypocenter. (b) Moment rates and their Fourier spectra are shown for the three directivity models (considering the same subsource distribution). In the spectral plot, the Brune's model spectrum (Brune, 1970) with stress drop of 1 MPa is shown. (c) Snapshots of the rupture propagation at two time instances for the three directivity models. (d) Apparent moment rate functions (top) and apparent source acceleration spectra (bottom) for the three directivity models at two stations lying in the forward (left) and backward (right) directivity regions.

▲ **Figure 4.** Comparison of observed and synthetic velocity waveforms in broad frequency range (0.05–5 Hz) as obtained by the RIK model in the weak-directivity mode (see the Model Description section for details). For the other directivity models, see Ⓔ Figure S1. Station names are to the left (see Fig. 1 for their location).

well by the model. The shorter-period content of the F-P components at stations 1765, N019B, N016, and 68150 is predicted as well. Interestingly, the model also correctly captures the presence of the dominant broad pulse at the F-P component and weaker F-N component at station NHC, which lies nearest to the hypocenter.

The more distant stations NGVB, NSP, and NTO have longer duration of the strong-motion phase and more rich spectral content at all components. Again, the model fits these recordings relatively well, despite the fact that these stations are more affected by the complexity of the wave propagation (see the overestimated later phases at the F-P components). Unfortunately, the stations in the backward-directivity zone (N002 and 68310) lie at relatively large distances. In particular, station N002 is dominated by the long duration of almost monochromatic oscillations clearly related to some basin effects. Nevertheless, the model fits the duration of the earlier part with higher frequency content. At station 68310 the model captures the position of the maximum peak at the F-N component, while it exceeds the amplitudes of the later long-period arrivals.

Figure 5a shows the comparison of the synthetics (red curves) with the observed data (black curves) in terms of the Fourier spectrum. The observed data were tapered at 20 s after

the hypocentral time to effectively remove spectral contributions due to the later low-frequency oscillations related to the unmodeled propagation effects. For clarity of the presentation, the spectra are smoothed by the Konno and Omachi (1998) method. In Figure 5a, I show only the vertical component as an example; for the other components, see Ⓔ Figure S2. With few exceptions, one can see that, generally, the modeled spectrum (red) follows the observed spectral fall-off. At some cases, the synthetic spectra underestimate the observed ones at frequencies > 1 Hz (e.g., N68150, NGVB). The worst situation is at station 68310, where the observed spectrum is significantly underestimated at frequencies > 0.5 Hz, although at low frequencies the model performs relatively well. I ascribe this problem to the radiation pattern effect that is in reality weakened at higher frequencies due to the 3D wave-propagation effects as suggested by numerical modeling in random media (e.g., Gallovič et al., 2010; Imperatori and Mai, 2012).

Figure 5b shows the modeling bias (red crosses) in terms of PGV defined as the natural logarithm of the ratio between the observed and modeled PGV. The figure also shows mean values and standard deviations evaluated over the stations for the individual components (the outlying large bias at vertical component of the 68310 station has been removed from this calculation). I emphasize that the bias is close to the zero line (corresponding to perfect fit) with very low standard deviation (0.02–0.26). Figure 6 (left column) then displays the modeling bias in terms of the acceleration response spectra at the individual components. The mean bias (black curve) is close to zero at the F-N component. At the others, the bias suggests minor underestimation (−0.3). The variance of the bias is also rather low (0.2–0.4), especially at the F-N component.

Modeling the Strength of the Observed Directivity Effect

Here, I discuss the modeling bias when the other two strengths of the directivity effect are considered. I remind the reader that Figure 3 shows properties of the three directivity models in terms of the moment rate functions, rupture propagation snapshots, and the apparent source time functions. Ⓔ Figures S1 and S2 display all simulated velocity waveforms and their smoothed Fourier spectra, respectively, for all the directivity models.

Figure 5a illustrates the effects of the directivity strength on the Fourier spectra. Major differences between the directivity models are visible mostly at the forward-directivity stations (top four panels in Fig. 5a), where the strong directivity leads to clear overestimation of the observed spectra at frequencies > 1 Hz. This is also evident in Ⓔ Figure S1c as too-strong high-frequency oscillations. At the other stations, the differences are also significant. At the backward-directivity station N002, the strongest amplitudes are predicted by the strong-directivity model. I assign this to the up-dip rupture propagation that amplifies the N002 synthetics. Indeed, at station 68310, which is not affected by the up-dip propagation, the largest Fourier amplitudes are obtained by the model with the weakest directivity. Overall, both the weak- and moderate-directivity models perform similarly well.

(a) Smoothed velocity spectra (vertical componet)

(b) PGV bias
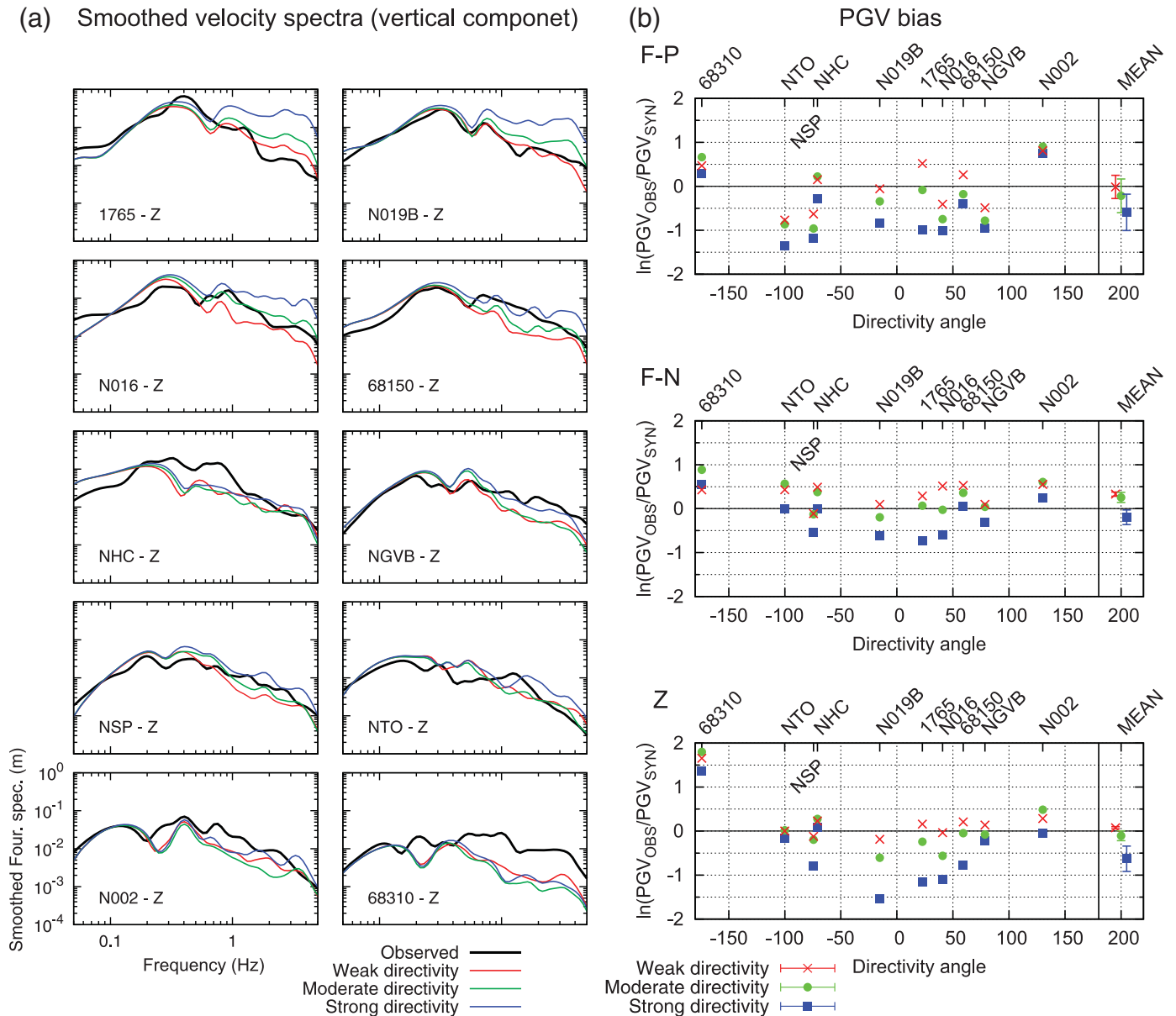
▲ **Figure 5.** Result of the broadband velocity waveform modeling using the RIK model in the three directivity modes (see legend). (a) Comparisons of the directivities in terms of the smoothed Fourier spectra at the individual stations (vertical component) are shown. For the other components, see Ⓔ Figure S2. (b) Modeling bias is shown in terms of peak velocities (PGV), defined as the natural logarithm of the ratio of the observed and synthetic PGV plotted as a function of the directivity angle (i.e., clockwise-positive angle from the antistrike direction) for the three directivity models (shaded). The mean and standard deviation evaluated over each station component are shown with error bars (denoted as MEAN). The Z component of station 68310 has been removed from the mean and variance calculations as an outlier.

Figures 5b and 6 display the modeling bias for all the directivity models in terms of PGV and response spectra, respectively. As one can see, especially the strong-directivity model clearly overestimates the observed data, which is expressed by the negative values of the mean bias. The moderate- and weak-directivity models perform better in this sense. In particular, the moderate-directivity model shows slightly better fit at F-N and Z components, whereas the F-P component is fitted better by the weak-directivity model. I point out that underprediction at high frequencies is preferable because the site

effects are rather underestimated here, considering only a generic soft-rock properties.

I emphasize that when discussing the performance of the individual models in modeling the directivity effect, one needs to consider mainly the variability of the bias (modeling variance) over the stations, keeping in mind that the directivity affects the waveforms systematically in the azimuthal sense. Although site effects would also contribute to the modeling variance, their involvement in the modeling would (statistically speaking) decrease the modeling variances but almost equally
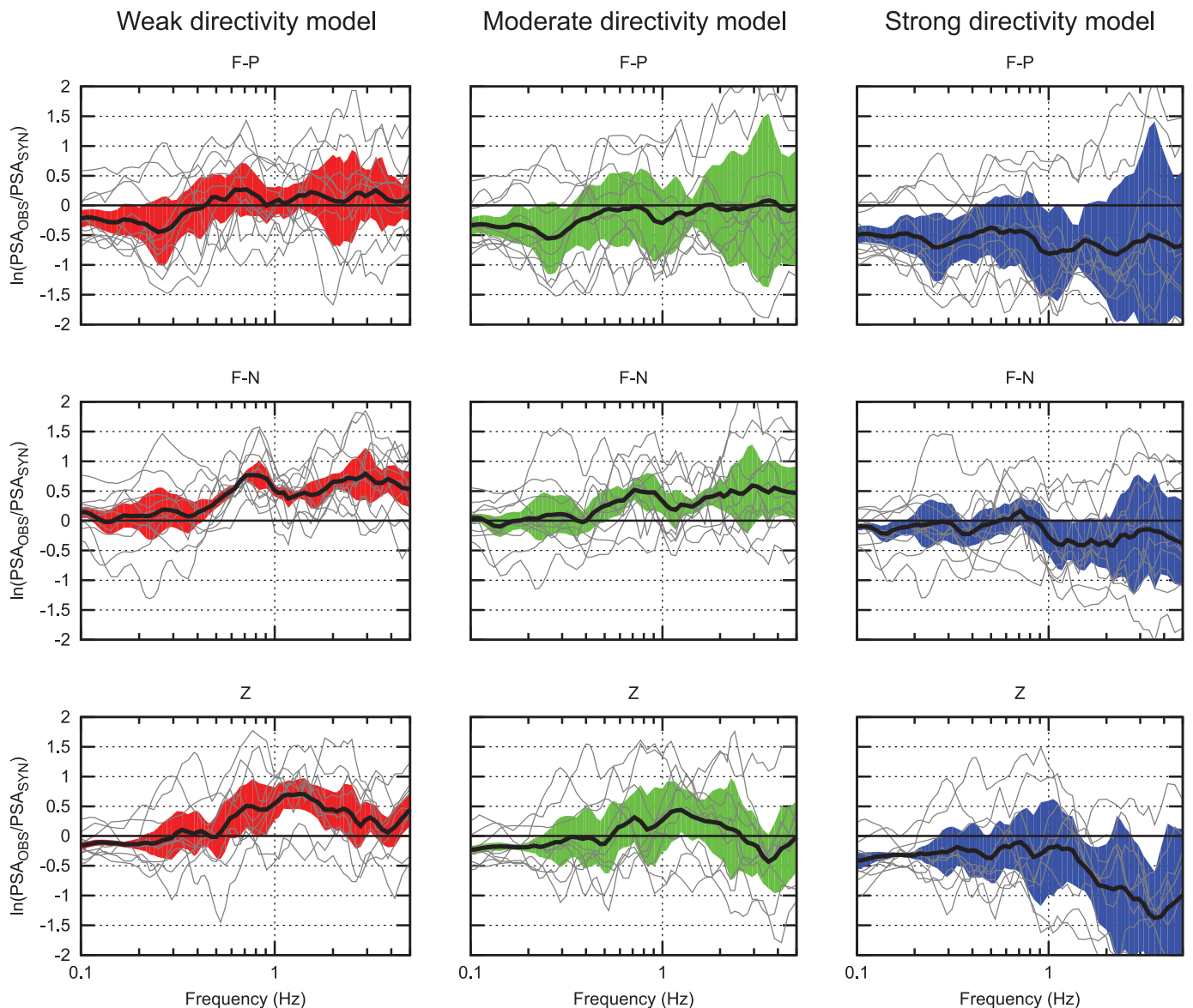
▲ **Figure 6.** Modeling bias in terms of acceleration response spectra, defined as the natural logarithm of the ratio of the observed and synthetic pseudospectral acceleration (PSA) plotted as a function of frequency for the three directivity models (columns) and individual components (rows). Gray lines correspond to the modeling bias at the individual stations. The black line and shaded strip denote the mean over stations and ± 1 standard deviation, respectively. Shades distinguish the directivity models as in Figure 5. The Z-component for station 68310 was removed from the mean and variance calculations as an outlier. (Abbreviations are as in Fig. 2.)

for all the directivity models. In particular, the variability of the modeling bias across the stations (expressed by the error bars in Fig. 5b and shaded strips in Fig. 6) is consistently smallest for the weak-directivity model. The moderate-directivity model provides the bias variance similar to the weak-directivity model but only at the F-N component. The strong-directivity model clearly overestimates the directivity as expressed by the largest modeling variance. I note that the strong-directivity model cannot be improved by decreasing the rupture velocity. Indeed, the required reduction of the rupture velocity to diminish the forward-directivity effect would lead to significant overestimation of the durations of the observed velocity pulses. Thus, I

conclude that the strong-directivity model can be considered unrealistic. Although, of the three models, the weak-directivity model best explains the data in terms of modeling variance, the performance of the moderate-directivity model is also satisfactory. I emphasize that both the latter two models are characterized by a directivity effect that weakens with increasing frequency, which is a crucial feature to fit the observed records.

DISCUSSION AND CONCLUSIONS

In the present article, I performed a seismological analysis of the 2014 South Napa earthquake with the emphasis on its

directivity effect. Using the near-fault high-quality recordings, a slip inversion was performed (in the 0.05–0.5 Hz frequency range), retrieving up-dip and against-strike (northward) rupture propagation. The rupture is characterized by a major slip patch located at depths shallower than 5 km. I note that, although the source model is rather smooth with respect to the other published models (Dreger *et al.*, 2015; Ji *et al.*, 2015; Wei *et al.*, 2015), it is robust in terms of quality of the crustal model considered, not requiring use of any artificial time shifts of the GFs. The inferred slip model is used to constrain a broadband (0.05–5 Hz) source model to predict the velocity waveforms. Specifically, I have considered the RIK model introduced by Ruiz *et al.* (2011). It is characterized by the k^{-2} slip distribution and the k-dependent rise time, correctly providing the omega-squared spectral decay at high frequencies (see Ruiz *et al.*, 2011). The advantage of this model is that one may control the strength of the directivity effect, including its frequency dependence by considering the rupture propagation as more (or less) coherent. In particular, I have considered three models with weak-, moderate-, and strong-directivity effects. The first two models are characterized by decreasing strength of the directivity effect with increasing frequency.

The weak- and moderate-directivity models are shown to best fit the observed velocity waveforms in both the temporal domain (Fig. 4), including the peak values (Fig. 5b), and in terms of the response spectra (Fig. 6). Those two models explain the observed data with both the smallest modeling bias and modeling variance (variability of the bias over stations). This is particularly important because any mismodeling of the directivity effect of this unilateral event introduces a systematic azimuthally dependent variability in the modeling bias, thus increasing the modeling variance. In this sense, the weak-directivity model fits the data slightly better than the moderate-directivity model. Because of the very large modeling variance, the strong-directivity model can be confidently considered as unrealistic.

All three models have rise time proportional to the reciprocal to the local rupture velocity and to the spatial scale of slip. Therefore, rise times are largest at the shallow asperity, as also observed by Ji *et al.* (2015) and Wei *et al.* (2015). However, this feature alone cannot explain the observed weak high-frequency directivity, because only the weak- and moderate-directivity models are able to model correctly the low-frequency directivity pulses observed at the forward-directivity stations while not overpredicting the high-frequency spectral content. The models have rupture speed corresponding to 80% of the depth-dependent shear-wave velocity (see Table 1), which is almost the same value as inferred by other authors (e.g., Dreger *et al.*, 2015; Wei *et al.*, 2015). Such a large rupture velocity would lead to very strong amplification at high frequencies if a coherent rupture is considered as illustrated by the strong-directivity model. The weak- and moderate-directivity RIK source models are characterized by complex style of rupture propagation at short wavelengths, leading to the weakening of the directivity effect at high frequencies. The weak high-frequency directivity

model thus explains the weak imprint of the rupture directivity in the ShakeMaps, despite the mostly unilateral character of the rupture propagation. Furthermore, it also potentially explains the observed frequency dependence of the residuals with respect to GMPEs analyzed by Baltay and Boatwright (2015); see also the Introduction.

The modeling is based on a relatively complex source model embedded in a 1D wave-propagation medium. I admit that the 1D wave-propagation model is a significant simplification, which, on the other hand, allows for extensive tests because the computational cost is rather small (approximately three days to calculate GFs on a common personal computer, and then just minutes to generate the RIK slip rates and evaluate the representation integral for each source model). This way, because the source model is built upon characteristics inferred by the slip inversion, the modeling allows for identification of features in the broadband observed waveforms that can be ascribed to the source effects. Indeed, while the later arrivals are not captured by the model (being presumably induced by 3D crustal heterogeneities), the early parts of displacement and velocity waveforms are explained relatively well. Indeed, Dreger *et al.* (2015) and Wei *et al.* (2015) analyzed effects of the 3D medium on the South Napa earthquake synthetics (up to 1 Hz), demonstrating mostly amplification of the vertical components (up to approximately two to three times) and occurrence of later phases at more distant stations. At the near-fault stations, the first pulses at most of the horizontal components are not altered significantly. In some cases (e.g., station 1765), the 3D velocity model slightly improves the fit, whereas at others the 3D medium does not help to explain the data. Because these effects are dependent on the actual source model, in a future study I plan to combine the source model developed here with the wave propagation in a complex 3D crustal model (including random heterogeneities and topography at short scales) to explore its effects on the present source model. Nevertheless, although I expect that taking into account the complexity of the velocity structure will improve the modeling bias, the modeling variance will change for all the three models in the same way, thus preserving my conclusions regarding the frequency dependence of the directivity.

Another simplified aspect of the source models of this study is related to the simplified west-dipping planar fault model geometry as adopted from the CMT solution of Berkeley. Other authors use different fault geometries, including those dipping east and/or consisting of two segments, as suggested by the observed surface ruptures (Wei *et al.*, 2015). We tested other fault geometries in the slip inversion, always obtaining a similar data fit but with more pronounced ghost features in the inferred slip rates. The impact on the RIK modeling has not been extensively studied yet. Although the fault geometry will have some effect on the velocity synthetics (perhaps eventually improving the modeling bias), I expect that it will affect the modeling variance of all three models in the same way, thus preserving the directivity-related conclusions as discussed also above in the case of the 3D velocity model. Nevertheless, this aspect also deserves further study.

The RIK source model is characterized by complex style of rupture propagation especially at short wavelengths, which leads to weakening of the directivity effect at high frequencies. I note that the present model is not unique in providing synthetics with the weak high-frequency directivity effect. Widely and successfully used source models for strong-motion simulations utilizing the so-called composite modeling at high frequencies (Zeng *et al.*, 1994; Pitarka *et al.*, 2000; Gallovič and Brokešová, 2007) implicitly consider no or very weak directivity effect at high frequencies (Gallovič and Burjánek, 2007). Analysis of observed spectra by Somerville *et al.* (1997) suggested that the strength of the directivity effect decreases with increasing frequency. Fletcher (2014) observed such a frequency-dependence of the directivity in the USGS Parkfield Seismic Array recordings of the 2004 Parkfield earthquake. By means of broadband modeling of the 2009 M_w 6.3 L'Aquila earthquake recordings, Ameri *et al.* (2012) showed that the observed directivity effect is reduced significantly already at frequencies > 0.5–2 Hz (depending on the station fault distance). All this thus suggests that the feature of the rather weak source directivity is unique to the 2014 South Napa, but is perhaps common to other earthquakes. Interestingly, similar behavior of the frequency-dependent directivity effect was observed by Day *et al.* (2008) in laboratory foam rubber experiments simulating earthquake with a unilateral rupture propagation. Day *et al.* (2008) discussed possible rheological features that may be responsible for considerable complexity of the rupture propagation. Those are, for example, localized strong barriers that initially withstand the main rupture front arrival and break later with rupture propagation direction even different from that of the main rupture front, as in the RIK model (see also laboratory experiments by Latour *et al.*, 2013). Such barriers can be also formed by irregularities in the fault geometry (Shi and Day, 2013) that are not included in our simulations and might represent another extension of the present work.

DATA AND RESOURCES

Accelerometric data were downloaded from the freely available online repository, Center for Engineering Strong Motion Data (CESMD, http://strongmotioncenter.org, last accessed October 2015). The ShakeMap shown in Figure 1 was downloaded from its archive (http://www.quake.ca.gov/shake/archive/, last accessed October 2015). Location parameters were taken from the U.S. Geological Survey Earthquake Location Archive (http://earthquake.usgs.gov, last accessed October 2015). Earthquake mechanism was adopted from the Northern California Earthquake Data Center (http://www.ncedc.org/, last accessed October 2015). ⧖

ACKNOWLEDGMENTS

REFERENCES

Ameri, G., F. Gallovič, and F. Pacor (2012). Complexity of the M_w 6.3 2009 L'Aquila (central Italy) earthquake: 2. Broadband strong motion modeling, *J. Geophys. Res.* **117,** no. B04308, doi: 10.1029/2011JB008709.

Andrews, D. J. (1980). A stochastic fault model: 1. Static case, *J. Geophys. Res.* **85,** 3867–3877.

Baltay, A., and J. Boatwright (2015). Ground motion observations of the 2014 South Napa earthquake, *Seismol. Res. Lett.* **86,** 355–360.

Baltay, A. S., and T. C. Hanks (2014). Understanding the magnitude dependence of PGA and PGV in NGA-West2 data, *Bull. Seismol. Soc. Am* **104,** 2851–2865.

Barnhart, W., J. R. Murray, S.-H. Yun, J. L. Svarc, S. V. Samsonov, E. J. Fielding, B. A. Brooks, and P. Milillo (2015). Geodetic constraints on the 2014 M 6.0 South Napa earthquake, *Seismol. Res. Lett.* **86,** 335–343.

Bernard, P., A. Herrero, and C. Berge (1996). Modeling directivity of heterogeneous earthquake ruptures. *Bull. Seismol. Soc. Am.* **86,** 1149–1160.

Bouchon, M. (1981). A simple method to calculate Green's functions for elastic layered media, *Bull. Seismol. Soc. Am.* **71,** 959–971.

Brocher, T. M., A. S. Baltay, J. L. Hardebeck, F. F. Pollitz, J. R. Murray, A. L. Llenos, D. P. Schwartz, J. L. Blair, D. J. Ponti, J. J. Lienkaemper, *et al.* (2015). The M 6.0 24 August 2014 South Napa earthquake, *Seismol. Res. Lett.* **86,** 309–326.

Brune, J. N. (1970). Tectonic stress and the spectra of seismic shear waves from earthquakes, *J. Geophys. Res.* **75,** 4997–5009.

Coutant, O. (1989). Program of numerical simulation AXITRA, *Research Report*, Laboratoire de Géophysique Interne et Tectonophysique, Université Joseph Fourier, Grenoble, France.

Day, S. M., S. H. Gonzalez, R. Anooshehpoor, and J. N. Brune (2008). Scale-model and numerical simulations of near-fault seismic directivity, *Bull. Seismol. Soc. Am.* **98,** no. 3, 1186–1206.

Dobry, R., R. D. Borcherdt, C. B. Crouse, I. M. Idriss, W. B. Joyner, G. R. Martin, M. S. Power, E. E. Rinne, and R. B. Seed (2000). New site coefficients and site classification system used in recent building seismic code provisions, *Earthq. Spectra* **16,** 41–67.

Dreger, D. S., M.-H. Huang, A. Rodgers, T. Taira, and K. Wooddell (2015). Kinematic finite-source model for the 24 August 2014 South Napa, Califonia, earthquake from joint inversion of seismic, GPS and InSAR data, *Seismol. Res. Lett.* **86,** 327–334.

Fletcher, J. B. (2014). Frequency-dependent effects of rupture for the 2004 Parkfield main shock, results from UPSAR, *J. Geophys. Res.* **119,** 7195–7208.

Gallovič, F., and J.-P. Ampuero (2015). A new strategy to compare inverted rupture models exploiting the eigen-structure of the inverse problem, *Seismol. Res. Lett.* **86,** doi: 10.1785/0220150096.

Gallovič, F., and J. Brokešová (2004). On strong ground motion synthesis with k^{-2} slip distributions, *J. Seismol.* **8,** 211–224.

Gallovič, F., and J. Brokešová (2007). Hybrid k-squared source model for strong ground motion simulations: Introduction, *Phys. Earth Planet. In.* **160,** 34–50.

Gallovič, F., and J. Burjánek (2007). High-frequency directivity in strong ground motion modeling methods, *Ann. Geophys.* **50,** 203–211.

Gallovič, F., W. Imperatori, and P. M. Mai (2015). Effects of three-dimensional crustal structure and smoothing constraint on earthquake slip inversions: Case study of the M_w 6.3 2009 L'Aquila earthquake, *J. Geophys. Res.* **120,** 428–449.

Gallovič, F., M. Käser, J. Burjánek, and Ch. Papaioannou (2010). Three-dimensional modeling of near-fault ground motions with nonplanar rupture models and topography: Case of the 2004 Parkfield earthquake, *J. Geophys. Res.* **115,** no. B03308, doi: 10.1029/2008JB006171.

Grapenthin, R., I. Johanson, and R. M. Allen (2014). The 2014 M_w 6.0 Napa earthquake, California: Observations from real-time GPS-enhanced earthquake early warning, *Geophys. Res. Lett.* **41,** 8269–8276.

Graves, R. W., and A. Pitarka (2010). Broadband ground-motion simulation using a hybrid approach, *Bull. Seismol. Soc. Am.* **100,** 2095–2123.

Imperatori, W., and M. P. Mai (2012). Broad-band near-field ground motion simulations in 3-dimensional scattering media, *Geophys. J. Int.* **192,** 725–744.

Ji, Ch., R. Archuleta, and C. Twardzik (2015). Rupture history of 2014 M_w 6.0 South Napa earthquake inferred from near fault strong motion data and its impact to the practice of ground strong motion prediction, *Geophys. Res. Lett.* **42,** 2149–2156.

Kennett, B. L. N., and N. J. Kerry (1979). Seismic waves in a stratified half space, *Geophys. J. Int.* **57,** 557–583.

Konno, K., and T. Omachi (1998). Ground-motion characteristics estimated from spectral ratio between horizontal and vertical components of microtremor, *Bull. Seismol. Soc. Am.* **88,** 228–241.

Latour, S., C. Voisin, F. Renard, E. Larose, S. Catheline, and M. Campillo (2013). Effect of fault heterogeneity on rupture dynamics: An experimental approach using ultrafast ultrasonic imaging, *J. Geophys. Res.* **118,** 5888–5902.

Lawson, C. L., and R. J. Hanson (1974). *Solving Least Square Problems*, Prentice-Hall, Upper Saddle River, New Jersey, 340 pp.

Melgar, D., J. Geng, B. W. Crowell, J. S. Haase, Y. Bock, W. C. Hammond, and R. M. Allen (2015). Seismogeodesy of the 2014 M_w 6.1 Napa earthquake, California: Rapid response and modeling of fast rupture on a dipping strike-slip fault, *J. Geophys. Res.* **120,** 5013–5033.

Pitarka, A., P. G. Somerville, Y. Fukushima, T. Uetake, and K. Irikura (2000). Simulation of near-fault ground motion using hybrid Green's functions, *Bull. Seismol. Soc. Am.* **90,** 566–586.

Ruiz, J. A., D. Baumont, P. Bernard, and C. Berge-Thierry (2011). Modeling directivity of strong ground motion with a fractal, k^{-2}, kinematic source model, *Geophys. J. Int.* **186,** 226–244.

Schmedes, J., R. J. Archuleta, and D. Lavallée (2010). Correlation of earthquake source parameters inferred from dynamic rupture simulations, *J. Geophys. Res.* **115,** no. B03304, doi: 10.1029/2009JB006689.

Shi, Z., and S. M. Day (2013). Rupture dynamics and ground motion from 3-D rough-fault simulations, *J. Geophys. Res.* **118,** 1122–1141.

Sokos, E., A. Kiratzi, F. Gallovič, J. Zahradník, A. Serpetsidaki, V. Plicka, J. Janský, J. Kostelecký, and G.-A. Tselentis (2015). Rupture process of the 2014 Cephalonia, Greece, earthquake doublet (M_w 6) as inferred from regional and local seismic data, *Tectonophysics* **656,** 131–141.

Somerville, P., N. F. Smith, W. Graves, and N. Abrahamson (1997). Modification of empirical strong ground motion attenuation relations to include the amplitude and duration effects of rupture directivity, *Seismol. Res. Lett.* **68,** 199–222.

Stidham, C., M. Antolik, D. Dreger, S. Larsen, and B. Romanowicz (1999). Three-dimensional structure influences on the strong motion wavefield of the 1989 Loma Prieta earthquake, *Bull. Seismol. Soc. Am.* **89,** 1184–1202.

Wei, S., S. Barbot, R. Graves, J. J. Lienkaemper, T. Wang, K. Hudnut, Y. Fu, and D. Helmberger (2015). The 2014 M_w 6.1 South Napa earthquake: A unilateral rupture with shallow asperity and rapid afterslip, *Seismol. Res. Lett.* **86,** 344–354.

Zeng, Y., J. Anderson, and G. Yu (1994). A composite source model for computing realistic synthetic strong ground motions, *Geophys. Res. Lett.* **21,** 725–728.

František Gallovič
Charles University in Prague
Faculty of Mathematics and Physics
Department of Geophysics
V Holešovičkách 2
180 00 Praha 8, Czech Republic
gallovic@karel.troja.mff.cuni.cz